Two-component modeling of Strong Gravitational Lenses

A Thesis

submitted to

Indian Institute of Science Education and Research, Pune

in partial fulfillment of the requirements for the

BS-MS Dual Degree Programme Programme

by

Shreeja Gajanan Ghugal

under the guidance of

Prof. Masamune Oguri

Department of Physics, University of Tokyo

INDIAN INSTITUTE OF SCIENCE AND RESEARCH

PASHAN, PUNE 411008, INDIA

April 2022

This thesis is dedicated to my parents

For their endless support, love and encouragement

Certificate

This is to certify that this dissertation entitled **Two-component modeling of Strong Gravitational Lenses** towards the partial fulfilment of the BS-MS dual degree programme at the Indian Institute of Science Education and Research, Pune represents work carried out by **Shreeja Gajanan Ghugal** at Indian Institute of Science and Research, Pune under the supervision of **Prof. Masamune Oguri**, Department of Physics, University of Tokyo during the academic year **2021-2022**

Supervisor

Prof. Masamune Oguri

Declaration

I hereby declare that the matter embodied in the report entitled **Two-component modeling of Strong Gravitational Lenses** are the results of the work carried out by me at the Department of Physics ,Indian Institute of Science and Research, Pune , under the supervision of **Prof. Masamune Oguri** and the same has not been submitted elsewhere for any other degree.

Student

Shreeja Gajanan Ghugal

Acknowledgements

I want to express my deep gratitude to Prof. Masamune Oguri, my supervisor, for his patient guidance and valuable critiques of this research work. I want to express my special gratitude to Dr. Kenneth Wong for contributing to this project. I want to thank Dr. Anupreeta More for her suggestions during the project. I thank my expert Dr. Arun Thalapillil for accepting to be a part of the thesis advisory committee.

I would also like to thank the Indian Institute of Science Education and Research, Pune for providing me with a platform where I could work in a research environment. Finally, I would like to thank the Government of India for providing me with the DST INSPIRE scholarship.

-

Contents

List of Figures ix

List of Tables xii

Abstract xv

1 Introduction 1

1.1 Gravitational Lensing . . . 1
1.2 Strong Gravitational Lensing . . . 1
1.3 Motivation . . . 2
1.4 Selection of the target systems . . . 3
1.5 Target System 1 - SDSSJ002927.38+254401.7 . . . 4
1.6 Target System 2 - *EYE OF HORUS* . . . 5
Cluster Environment of *Eye of Horus* . . . 6
1.7 Initial Mass Function . . . 7

2 Method 9

2.1 Obtaining Data . . . 9
2.2 Preparing Data For Strong Lensing Analysis . . . 10
2.3 Modeling . . . 10
2.3.1 Forward lens Reconstruction Method . . . 10
2.3.2 Lens Models . . . 11
Singular Isothermal Ellipsoid (SIE) Profile . . . 11
Power-Law (POW) Profile . . . 12
Hernquist (HERN) Profile . . . 12
Navarro–Frenk–White (NFW) Profile . . . 12
External Shear . . . 13

2.3.3 Source Models . . . 13
Sérsic Profile . . . 13
2.3.4 Point Spread Function(PSF) . . . 14
2.3.5 Sky Component . . . 14
2.3.6 Gravitational Lens Modeling Software . . . 15
glafic . . . 15
2.3.7 One-Component modeling . . . 15
2.3.8 Two-Component modeling . . . 15
2.3.9 Limitations and assumptions . . . 16
2.4 Evaluation of Model . . . 16
2.4.1 Chi-square minimization . . . 16
Degrees Of Freedom . . . 17

3 Results **19**
3.1 Single Source Plane System - SDSSJ002927.38+254401. . . . 19
3.1.1 One-Component Model . . . 19
Best-fit parameter values for this model . . . 20
Markov Chain Monte Carlo (MCMC) Analysis . . . 21
3.1.2 Two-Component Model . . . 22
Best-fit parameter values for this model . . . 23
3.1.3 Center and Shape of Mass Distributions . . . 24
3.1.4 Density Profiles . . . 25
3.2 Double Source Plane System - *Eye of Horus* . . . 26
3.2.1 One-Component Model . . . 26
Lens modeled using SIE profile . . . 26
Lens modeled using Power-law profile . . . 26
Best-fit parameter values for this model . . . 28
3.2.2 Two-Component Model . . . 30
Best-fit parameter values for this model . . . 30
3.2.3 Center and Shape of Mass Distributions . . . 32
3.2.4 Density Profiles . . . 34
3.2.5 Initial Mass Function . . . 34

4 Summary **35**

Bibliography **41**

List of Figures

1.1 Schematic diagram of double source plane lensing. Image credits: [1] . . . 4
1.2 The *riz* band combined color image of the *Eye of Horus* Image credits : [2] . 5
1.3 This figure gives an overview of the cluster environment of *Eye of Horus*. Image credits: [3] 6

2.1 Typical strong gravitationally lensed system. Image credit: ESA/Hubble NASA 10

3.1 The left panel corresponds to our best-fit model as per one-component modeling of the target system SDSSJ002927.38+254401.7 while the right panel is the actual HST image of the target system 20
3.2 The marginal posterior distributions for the lens parameters of Target 1 for one-component model 21
3.3 The left panel corresponds to our best-fit model as per two-component modeling of the target system SDSSJ002927.38+254401.7 while the right panel is the actual HST image of the target system 22
3.4 The marginal posterior distributions for the lens parameters of Target 1 for two-component model 24
3.5 Average Convergence vs Radius log-log Plot 25
3.6 The left panel corresponds to the actual HST image of the target system. Our best-fit model as per one-component modeling of the target system Eye of Horus is presented in middle panel, while the right panel is the residual image 28
3.7 The marginal posterior distributions for the lens parameters of the one-component model of *Eye of Horus* 29

3.8 The left panel corresponds to the actual HST image of the target system. Our best-fit model as per two-component modeling of the target system Eye of Horus is presented in middle panel, while the right panel is the residual image 30
3.9 The marginal posterior distributions for the lens parameters of the two-component model of the *Eye of Horus* 32
3.10 Average Convergence vs Radius log-log Plot 34

List of Tables

3.1 Lens parameters for the one-component model of Target 1 20
3.2 Source parameters for the one-component model of Target 1 21
3.3 Lens parameters for the two-component model of Target 1 23
3.4 Source parameters for the two-component model of Target 1 23
3.5 Parameter comparison of Hernquist (stellar) and NFW (dark matter) profile 24
3.6 Lens parameters for the one-component model of *Eye of Horus* 28
3.7 Source parameters for the one-component model of *Eye of Horus* 29
3.8 Lens parameters for two-component model of *Eye of Horus* 31
3.9 Source parameters for the two-component model of the *Eye of Horus* 31
3.10 Parameter comparison of the Hernquist (stellar) and NFW (dark matter) profile 32

Abstract

Determination of the mass distribution of various astrophysical objects is of utmost importance in multiple studies in astrophysics and cosmology. Strong gravitational lensing is a valuable tool in estimation of mass distributions of lensing objects. Generally, galaxy-scale strong lensing is analyzed assuming a single component for the lensing galaxy, such as a singular isothermal ellipsoid or a power-law ellipsoid. However, both stars and dark matter account for the mass of the lensing galaxy. This project explores two-component mass models of the lensing galaxy that consists of the stellar and dark matter components. Such accurate stellar and dark matter estimations are precious for testing the many models of structure formation and evolution.

We perform both one and two-component modeling on two strong gravitationally lensed systems. We model the first target system, SDSSJ002927.38+254401.7, selected from the BELLS GALLERY sample for training and understanding parameter degeneracies and other possible biases. Our principal target system is the double source plane lens system, *Eye of Horus*. Using the two-component modeling, we constrain the dark matter distribution of the foreground lensing galaxy within the Einstein radius. We also study the foreground lensing galaxy's density profile and initial mass function (IMF).

From one-component modeling, we find that the lensing galaxy of the *Eye of Horus* follows a power-law radial density profile ($\rho \propto r^{-\gamma}$) with $\gamma = 1.7559$. The stellar mass for the foreground lens is found to be $12.98 \times 10^{11} \mathrm{M}_{\odot}$. After comparing this with the stellar mass ($6.6 \times 10^{11} \mathrm{M}_{\odot}$) inferred from stellar population synthesis fitting, we find that a Salpeter IMF provides a good description of the stellar population of the foreground lens of *Eye of Horus*. After analyzing the two-component model of the *Eye of Horus*, the dark matter distribution is found to be more elongated than the stellar mass distribution. The next step towards getting a robust conclusion on shape comparison of the two mass distributions is to analyze two-component mass models of more such strong gravitationally lensed systems.

Chapter 1

Introduction

1.1 Gravitational Lensing

Gravitational lensing refers to the deflection of light when it propagates through a gravitational field, an effect that was predicted by Einstein's theory of Relativity and experimentally verified by Dyson et al. in 1919 when they measured the apparent angular shift of stars close to the limb of the Sun during a total solar eclipse.

There are three different types of gravitational lensing, each of which has its astrophysical applications: *Strong lensing*, where a large massive object like a galaxy or cluster of galaxies creates multiple images of a background source, and often an observer sees large deformations, i.e., arcs. *Weak lensing*, where the large-scale structure along the line of sight produces mildly distorted images of sources. These distortions cannot be identified in individual sources, but the shear can be measured statistically. *Microlensing*, where the lens is a low mass compact object like a star which creates multiple images that are currently unresolvable. In this thesis, we will use the phenomena of strong gravitational lensing [4].

1.2 Strong Gravitational Lensing

Strong gravitational lensing [1] is an important cosmological tool with various astrophysical applications. To name some, it is used to probe mass distributions of lenses and to obtain a precise estimation of values of cosmological parameters. In this thesis, we are focusing on

[1] Refer to [4–6] to learn more about gravitational lensing formalism and lensing related terms used in this thesis

galaxy-galaxy strong lensing. It is known that a significant fraction of the mass of galaxies comprise of dark matter [7] whose nature remains a mystery. Hence, understanding the interplay of baryons and dark matter and how they bring about the observed structural characteristics is important to learn about the evolution of early-type galaxies. Since dark matter is not directly visible and interacts only via gravity, gravitational lensing serves as a powerful tool in determining the distribution of dark matter in galaxies [8]. To be more precise, since the lensing geometry fixes the total mass within the Einstein radius [2] and stellar mass is constrained by the observed light profile of the lensing galaxy, it is possible to separate the two mass distributions and learn about dark matter fraction and its shape. The relative shape of the stellar mass distribution with respect to dark matter distributions in terms of ellipticity and position angle encompasses information about galaxy formation and the current cosmological model - Lambda cold dark matter (ΛCDM (e.g., [10, 11])). Therefore, it is important to study the shapes of the mass distributions, and strong lensing helps us to probe them.

We aim to use strong gravitationally lensed systems to constrain the dark matter distribution and its shape and study the density profile and Initial Mass Function (IMF) of the lensing galaxies present in the target systems selected for this thesis. Our focus is to model the target systems using two-component modeling.

1.3 Motivation

In most cases, galaxy-scale strong lensing is analyzed assuming a single component for the lensing galaxy, such as a Singular Isothermal Ellipsoid [12] or a Power-law Ellipsoid [13]. However, it is known that the lensing galaxy contains stellar and dark matter components, both of which contribute to the mass within the Einstein radius. In this project, we aim to explore two-component mass models of the lensing galaxy consisting of both the stellar and dark matter components.

[2] Refer footnote 1 for definitions and [9] as an example

The shape of the stellar mass component is constrained by the observed light profile of the lensing galaxy, while the dark matter distribution can take a flexible form. For the target galaxy-scale strong lensed systems, we will study how well the dark matter distribution can be constrained from two-component mass modeling. We believe that the shape of the dark matter distribution constrained by this method may provide valuable constraints on dark matter's particle nature, such as self-interaction. Exploring such flexible two-component mass models is essential also for more accurate time delay cosmography [14] from time-variable strong lenses such as lensed quasars and lensed supernovae, because currently the accuracy of time delay cosmography is largely limited by the mass modeling uncertainty.

1.4 Selection of the target systems

We perform mass modeling on two target systems. Our first target system is modeled with the aim of training for strong lensing modeling, so we choose a typical lens system that appears straightforward to model. We choose our central target system such that it has multiple arcs and many constraints on lens potential, which will help us successfully analyze the dark matter distribution.

Mass modeling of gravitationally lensed systems involves various parameters and model degeneracies. To break some of these degeneracies and obtain better constraints on the lens, we choose a Double Source Plane (DSP) lens system. DSP is a gravitationally lensed system, as shown in Figure 1.1, with two background sources at different redshifts that are aligned such that both split into multiple images. The presence of multiple sources and hence multiple arcs provide us an opportunity to better constrain the lens mass distribution. Double source plane systems are considered a valuable cosmological probe [15] for the dark matter distribution and IMF measurements [16]. They also provide us with a chance to explore the gravitational structure inside the lensing galaxy and make better estimates of cosmological parameters once mass-sheet degeneracy is broken (e.g., [17]) using the dynamical information (e.g., the velocity dispersion of the lens). One important quantity for DSP is the ratio of the two Einstein radii (corresponding to each source), which is independent of Hubble parameter (H_0) allowing us to break the degeneracy between H_0 and matter

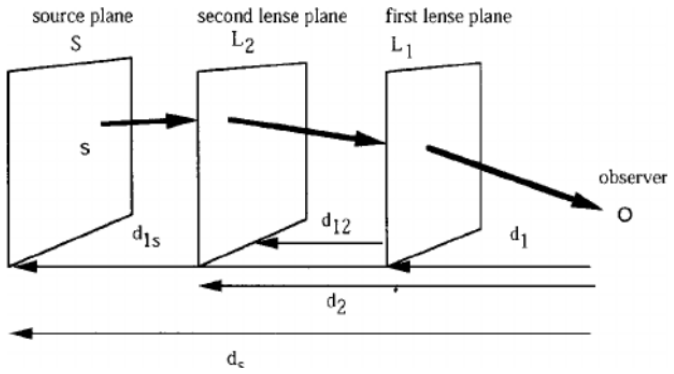

FIGURE 1.1: Schematic diagram of double source plane lensing.
Image credits: [1]

density parameter Ω_M and equation of state parameter ω [18, 19].

Double source plane systems are rare, and very few have been discovered to date (e.g., [20, 21]) . Also, since the second source of these systems is faint, their spectroscopic redshifts are not available. As a result it is important to choose a good DSP for analysis carefully.

For this thesis, we choose our trial system to be SDSSJ002927.38+254401.7 from BELLS GALLERY sample of THE BOSS EMISSION-LINE LENS SURVEY IV [22]. The central target system for our analysis is chosen to be the *Eye of Horus* [2], a DSP for which spectroscopic redshift measurements for both sources are available. Further details about these target systems are provided in the following two sections of this chapter.

1.5 Target System 1 - SDSSJ002927.38+254401.7

Target SDSSJ002927.38+254401.7 is a strong lens system selected from the BELLS GALLERY sample that was presented in [22]. The foreground lens galaxy is a massive early-type galaxy at redshift $z_{\mathrm{L}} = 0.5869$. The background source is Lyα emitter at redshift $z_{\mathrm{S}} = 2.4504$. This is a single source plane gravitationally lensed system.

1.6 Target System 2 - *EYE OF HORUS*

The Eye of Horus is a strong gravitationally lensed system named after the sacred eye of an ancient Egyptian deity due to its resemblance. It was discovered in 2015 at the National Astronomical Observatory of Japan by a team of undergraduate students and researchers while they were inspecting images from the Hyper Suprime-Cam Subaru Strategic Program (HSC-SSP survey) [2]. It is the first DSP system for which both source redshifts have been measured accurately. The foreground lens galaxy of this system is a massive early-type galaxy at the redshift z_L = 0.795, and its background source galaxies are at redshifts z_S = 1.302 and 1.988.

A pseudo color composite of images taken by Hyper Suprime-Cam on the 8.2-meter Subaru Telescope is presented in Figure 1.2. From Figure 1.2b, we can clearly distinguish the two different colored arcs located at the Einstein radius corresponding to each source, confirming that this is indeed a DSP system.

FIGURE 1.2: The *riz* band combined color image of the *Eye of Horus*
Image credits : [2]

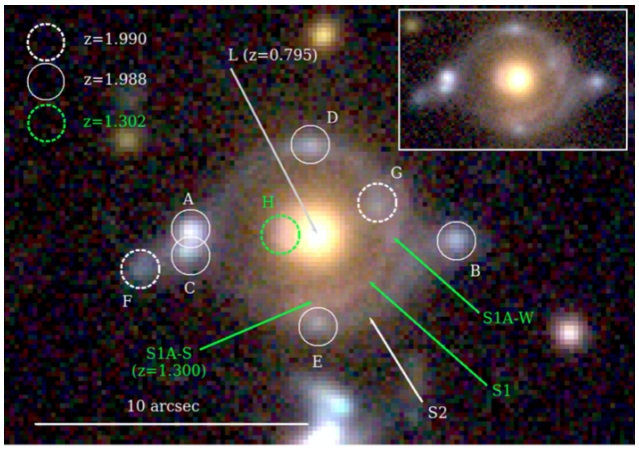

(A) The different important features of the lensed system are marked on this image, and their spectroscopic redshifts are presented on the top left corner.

(B) The lens is subtracted from the system in this image. The different colored arcs are now clearly visible.

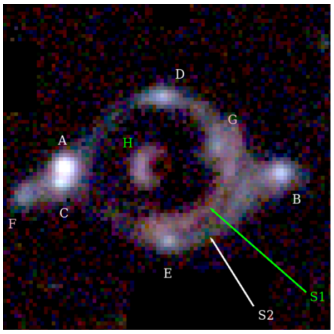

Important features of the *Eye of Horus* system can be analyzed using Figure 1.2a. We see that there are two different arcs; the inner arcs correspond to lensed images of the source 1 (S1) at z_S = 1.302, and the outer arcs ,i.e., features A, B, C, D, E, G, and F, correspond to the lensed images of source 2 (S2) at z_S = 1.988. There is an offset between the redshifts

of the features A-E and G-F, which indicates we will have to use multiple different source components while modeling the system. If we observe the left-hand side of the outer arc, we see a split of the image, resulting in features A and C. Better details of this structure can be seen in the Hubble Space Telescope (HST) image used for our modeling.. This split is believed to result from lensing by a satellite galaxy at redshift $z = 0.795$ present somewhere between these two features. There are several blobs/knots present in the arcs, which we will be modeling using several source components in the model. Further details are provided in the forthcoming chapters.

Cluster Environment of *Eye of Horus*

Mass modeling can be done accurately when the lensed system is isolated. But the lens galaxy of *Eye of Horus* is present in HSC J142449-005322 cluster ($z \sim 0.801$) which is part of the CAMIRA cluster catalog [23]. Other than this main cluster, it is also surrounded by another cluster ($z \sim 0.768$) located ∼100 arcsec north-east of it, as shown in Figure 1.3. The main cluster is about 100 times greater in mass than NE cluster when measured within the Einstein radius. Because clusters surround this system, we expect that the lensed images are affected by the cluster environment [24]. X-ray emissions were observed with *XMM– Newton* by [3] around this strong lens system to analyze the influence of the cluster environment. It was found that the main cluster located about 3.8 ± 1.0 arcsec south of the lens galaxy of the system contributed significantly to the total mass within the Einstein radius. On the other hand, the contribution from the other north-east cluster could be neglected. We see that the *Eye of Horus* has a complex gravitational structure around it as well as maybe along the line of sight, and hence we refer to this information while analyzing the system henceforth.

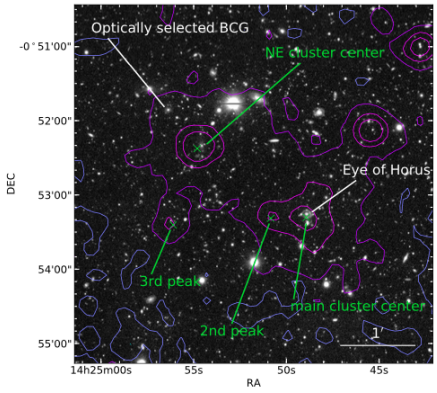

FIGURE 1.3: This figure gives an overview of the cluster environment of *Eye of Horus*.
Image credits: [3]

1.7 Initial Mass Function

The stellar initial mass function (IMF) is a function that describes the initial distribution of masses for the stellar population of galaxies. It holds the key to understanding and modeling star formation and galaxy evolution. Though theory suggests varying IMF owing to different star-formation conditions, observations of the local universe confirm invariant IMF. Hence, a robust study on IMF is essential. Generally, a universal, non-evolving IMF such as Salpeter [25] or Chabrier [26] IMF is assumed for the early-type galaxies. Salpeter IMF gives s $\sim$2 $\times$ stellar mass than the Chabrier IMF. In this study, we compare the stellar mass derived from our lensing models with the stellar mass derived from the stellar mass synthesis fitting to analyze the IMF of the foreground lens of the target systems.

Chapter 2

Method

This chapter presents the method we used to model the two target systems, BELLS GALLERY grade-A lens SDSSJ002927.38+254401.7 (Target 1, Section 1.5) and EYE OF HORUS (Section 1.6). Sections 2.1 and 2.2 describe our method to obtain telescope images of the target systems. Sections 2.3 and 2.4 introduce the modeling technique and software that we used in this thesis.

2.1 Obtaining Data

In our thesis, we model the target systems based on their Hubble Space Telescope (HST) images. The data of each target system has to be downloaded from the Mikulski Archive for Space Telescopes (MAST)[1], which is an archive of astronomical data. To do this, we develop a code that can be customized to download the FITS files containing data of exposures from the different camera/filter combinations from every visit of HST, of any target system.

Once we have all the relevant files, we apply the drizzle operation on the data using AstroDrizzle of DrizzlePac software package. The Drizzle algorithm [27] is a powerful method for combining dithered HST images, i.e., images (exposures) observed with different pointings (offsets). Various tasks like aligning, distortion-correcting, cosmic-ray cleaning, and combining HST images are performed by astrodrizzle. Once this operation is completed, we get a combined image of our target systems. Our thesis adopts the combined image corresponding to the F606W filter for the analysis since it very well encompasses all the lensed features.

[1] Details of HST imaging are provided here

2.2 Preparing Data For Strong Lensing Analysis

The combined images cover data corresponding to a large area over space, whereas we are interested in just our target system. Hence we further work on the data to get the cutout of our target system, which is correctly oriented, and the size is adjusted to avoid surrounding objects. We also extract the noise map for our final cutout image. The cutout size details are provided in Chapter 3

2.3 Modeling

Lens reconstruction of strong gravitationally lensed systems constrains the lens mass distribution owing to the requirement that multiply-imaged points on the image trace back to the same source plane location, and through the relative magnifications of the individual images. The lens is constrained by data points over continuous regions when multiple extended images are present in observation of the target system. Figure 2.1 shows an example of strong gravitationally lensed system that contains large arcs which contain abundant information to constrain the lens mass distribution.

FIGURE 2.1: Typical strong gravitationally lensed system.
Image credit: ESA/Hubble NASA

The modeling problem, in general, can be divided into either a forward or reverse problem. We have used the forward lens reconstruction method in our thesis.

2.3.1 Forward lens Reconstruction Method

This method of modeling tries to create a model of the gravitationally lensed system that reproduces the observation image of the system as accurately as possible.

The method comprises of following steps.

1. A parameterized model of the lensed system, i.e., sources and lenses, is defined using known mass and light distribution profiles.
2. Model is simulated to obtain an image.
3. Predicted image is compared to the data.
4. Model is changed according to the results.

Since an educated guess about the parameter values of the mass distribution has to be made in such a modeling approach, it is sometimes considered disadvantageous over the reverse problem. However, the results of this method are relatively easy to interpret since the parametric models use a physical basis to describe the lens and source components. Another advantage is the direct control over the model, so we choose this analysis method.

2.3.2 Lens Models

The forward method's simulation and reconstruction of galaxy-scale lenses is done by a model consisting of a combination of N_L number of parametric lens mass components. The mass profiles of these components are selected from the catalog of mass models (e.g. [28]) according to the requirement. This section briefly introduces the mass profiles used for modeling in this thesis.

Singular Isothermal Ellipsoid (SIE) Profile

The density profile for axisymmetric Singular Isothermal Sphere (SIS) is given by

$$\rho(r) = \frac{\sigma_v^2}{2\pi G}\frac{1}{r^2} \tag{2.1}$$

where σ_v is velocity dispersion of the stars. Projecting this density along the line of sight we get the following surface mass density

$$\Sigma(\xi) = \frac{\sigma_v^2}{2\pi G\xi} \tag{2.2}$$

where ξ is the magnitude of the two-dimensional vector on the lens plane. We know that lenses cannot always be circular, so we assume a generalized elliptical profile for our model i.e Singular isothermal ellipsoid (SIE) [12, 28]. When the mass profile is generalized to consider angular structure, for a lens with axis ratio q, the ellipticity is calculated as 1-q and the mass profile is given by replacing the radial coordinate ξ by $\sqrt{q^2\xi_1^2+\xi_2^2}$. SIE is the most commonly used profile to model the total mass distribution of lensing galaxies. This profile is parametrized using six parameters in this thesis. The parameters are lens redshift, velocity dispersion, position on both axes, ellipticity, and position angle.

Power-Law (POW) Profile

SIS is a part of the generalized lensing models called power-law lenses.The radial density for power-law profile $\rho(r) \propto r^{-\gamma}$ where $1 < \gamma < 3$ [29]. This profile is useful to find a better estimate of the radial density slope of the lensing galaxy. It is parametrized using eight parameters in this thesis. The parameters are lens redshift, source redshift position on both axes, ellipticity, position angle, einstein radius, and power index (γ).

Hernquist (HERN) Profile

This profile very well describes the light profile of early-type galaxies. The density profile for the Hernquist profile [30] is given by

$$\rho(r) = \frac{M_{tot}}{2\pi(r/r_b)(1+r/r_b)^3} \tag{2.3}$$

where M_{tot} is the total mass and r_b is scale radius. This profile is parametrized using seven parameters in this thesis. The parameters are lens redshift, mass, position on both axes, ellipticity, position angle, and scale radius.

Navarro–Frenk–White (NFW) Profile

The structure of dark matter halos seen in cosmological N-body simulations can be very well described by a universal density profile, the NFW profile [31] defined by

$$\rho(r) = \frac{\rho_s}{(r/r_s)(1+r/r_s)^2} \tag{2.4}$$

where ρ_s is characteristic density and r_s is the scale radius. This profile is parametrized using seven parameters in this thesis. The parameters are lens redshift, mass, position on both axes, ellipticity, position angle, and the concentration parameter, which is a ratio of virial and scale radii.

External Shear

The environment of the lens systems that are not isolated can break the symmetry of the main lens. Assuming that this perturbing gravitational field is constant over the lens length scale, the effect of the perturber at the lowest order can be considered as adding a constant convergence and tidal shear [2]. While modeling, we add lens components corresponding to external shear that are parametrized by shear strength and position angle. One issue in doing so is that there is often a parameter degeneracy between ellipticity of the mass profile of the lens and external shear, making it difficult to constrain the model correctly. Further details on the model are provided in the following chapters.

We mostly perform modeling using one to two lens mass components along with an external shear component. The light distribution of the lens is modeled using Sérsic profile described in the following section.

2.3.3 Source Models

The forward reconstruction method generally works with parametric light profiles of the sources. In this thesis, we use the following profile to describe all the source components of our models.

Sérsic Profile

The Sérsic profile is the prototypical profile for parametric sources and is widely used to describe light profiles of galaxies. It is given by

$$S(R) = \frac{L_\infty}{\pi R_{\rm eff}^2/q}\frac{b^{2n}}{\Gamma(2n+1)}\exp\left\{-b\left(\frac{R}{R_{\rm eff}}\right)^{1/n}\right\} \tag{2.5}$$

[2] Refer footnote 1

where the scale length R_{eff} is the half-light radius of the profile such that luminosity within radius R_{eff} is half of the total luminosity (L_∞).$n > 0$ is the Sérsic index of the profile. q is the axis ratio, and constant b is implicitly defined by $2\gamma(2n, b) = \Gamma(2n)$, where γ and Γ are respectively the lower incomplete Gamma function and Gamma function

This profile is determined by the seven parameters: the position on both axes, flux, Sérsic index n, axis ratio q, effective radius R_{eff}, and position angle θ. We use multiple Sérsic components while modeling to reproduce the lensed arcs in the system.

The Sérsic profile is a generalized model with special cases such as De Vaucouleurs profile (n = 4), exponential profile (n = 1), and Gaussian profile (n = 1/2) . Using this profile with indices in the range $1/2 < n < 10$, we can fit most of the galaxies. Sérsic index correlates n with galaxy luminosity and size, such that brighter and bigger galaxies tend to fit with larger n.

2.3.4 Point Spread Function(PSF)

The image is affected due to the instrument and ambient conditions. This is taken care of using the point-spread function (PSF), which represents what a true point source would look like in the data. The PSF for each target system of our project was created using TinyTim software [32]. A sanity check is conducted using the cutouts of two nearby bright stars extracted from the target systems' combined science image (i.e., before reduction to the cutout).

2.3.5 Sky Component

The diffused overall distribution of light, in other words, sky background, is often found in observations and must be included in the model during reconstruction. Flat surface brightness distribution with a constant value is the simplest model for the sky background. Even if the background noise has been subtracted in the preprocessing step, it is good to include the sky background as a free parameter in the model. In our thesis, we manually set the initial value of sky level and allow it to be optimized

2.3.6 Gravitational Lens Modeling Software

Software for modeling strong gravitational lensing can be divided into two subgroups: parametric and non-parametric models. The parametric lens models describe mass components by parameterized profiles. The non-parametric lens models are also parametric, but their parameters are the individual mass pixels. In our thesis we work with parametric lensing software *glafic* [33, 34].

glafic

glafic is public software package for analyzing gravitational lensing whose features include handling multi-plane lensing. It works by taking an input file which contains commands and information regarding the parameters for the model, the optimization method, initial priors for the profiles to be optimized, the cutout FITS file for the target system, PSF and the noise map. As output, *glafic* provides several files. Primarily we have a file containing the optimization results of model parameters and a FITS file corresponding to the best model parameters which can be then be analyzed using DS9 (image display and visualization tool for astronomical data) software.

2.3.7 One-Component modeling

One-component models in this thesis assumes a single component for the lensing galaxy, such as a singular isothermal ellipsoid (SIE) or a power-law ellipsoid (pow). Even though this thesis aims at two-component modeling of the target systems that gives us information about both stellar and dark matter distributions, we first perform one-component modeling on the systems.This is because two-component modeling is a computationally challenging task due to a greater number of parameters. Once we have the best model parameters from the simpler one-component modeling, the common model parameters are used as initial model parameters for the two-component modeling, making it more accurate and feasible.

2.3.8 Two-Component modeling

In this thesis, we model the stellar light distribution using the Hernquist profile [30] and dark matter distribution using the Navarro–Frenk–White (NFW) profile [31]. Further model

specific details are presented in the Chapter 3.

2.3.9 Limitations and assumptions

While performing one-component modeling, we assume an isothermal or a power law profile for the total lens mass distribution, despite the fact that it does not entirely describe either the baryons or the dark matter distribution. Similarly, we assume the Hernquist profile for stellar light distribution and NFW for dark matter distribution while two-component modeling, when in fact, these profiles are not the exhaustive choices and substructures of astronomical objects cannot be completely analyzed using these profiles. Our models are one of the good choices to model the target systems, and there can be other models which give similar results. Various model and parameter degeneracies can be found in this optimization process. We aim to find the best fit model that can cover all the system's main features.

2.4 Evaluation of Model

When we model the galaxy-galaxy strong lensing systems with parametric profiles and priors, we are trying to constrain the lens mass distribution using the lensed images of the background sources. In Section 2.4.1 we describe the optimization method used to get the best fit models in this thesis.

2.4.1 Chi-square minimization

To find the best fitting model, the Downhill Simplex method is used for optimization. We use the pixels in the predicted model image and compare them with the pixels in the data image, scaled by the variance of each pixel. The modeling procedure tries to minimize the difference between the two to find overall minimum χ^2. Strong gravitational lens modeling with this standard χ^2 minimization is time-consuming since many images and lens potential components are involved. Also, since in the beginning of the optimization we have to give the initial model parameters with the limited knowledge we have about the system it is possible that the position of the predicted and observed images differ substantially, which can be problematic. In order to overcome these problems we first evaluate χ^2 in the source plane to get some constraints on the lens and point source positions . Since there is no need

to solve the lens equation, the optimization is very fast though less accurate. These results from the point source fitting are then used as the initial parameters in the pixel by pixel fitting in the image plane. In addition to this, we build up our model gradually, adding new components only when we have minimized χ^2 for the current model.

Degrees Of Freedom

There is a control over which model parameters are to be optimized. Details about the free parameters of each model are given in Chapter 3. The degrees of freedom for a particular the system is calculated as

$$\text{D.O.F} = \text{Total number of pixels - Number of free parameters} \tag{2.6}$$

The reduced χ^2 for the model is calculated as

$$\text{Reduced } \chi^2 = \frac{\chi^2}{\text{D.O.F}} \tag{2.7}$$

and its value tending to 1 is considered a successful reconstruction.

The main issue with χ^2 minimization is the risk of hitting a local minimum and not finding the actual best model. To circumvent this problem, we perform Monte Carlo Markov Chain (MCMC) analysis on best fit model using glafic as part of our optimization routine.

We perform both one and two-component modeling on the target systems. The details of each model and results and presented in the next chapter.

Chapter 3

Results

We adopt the Hubble constant H_0 = 70 $kms^{-1}Mpc^{-1}$, the matter density $\Omega_M = 0.3$, and the cosmological constant $\Omega_\Lambda = 0.7$..

3.1 Single Source Plane System - SDSSJ002927.38+254401.

The cutout size of the images of this system is 125 $\times$ 125 pixels, and the pixel size is 0.0396 arcsec. We successfully perform one and two-component modeling on the Target SDSSJ002927.38+254401. One-component modeling of this system was done by Shu et al.(2016) [22]. We try to reproduce that result and additionally perform two-component modeling on this system.

3.1.1 One-Component Model

This model modeled the lens mass distribution using an SIE profile with external shear. The light profile of lens and source components are modeled using the Sérsic profile. We allow offsets between the position, ellipticity, position angle of the mass, and the light profile of the lens. The multiple arcs are modeled considering multiple source components, i.e., Sérsic components at the same redshift. It is found that three Sérsic components for the source light profile can cover all the system's main features. Sérsic indices for all components are kept as free variables during optimization.

As per our current best fit model, after optimizing parameters, we obtain the reduced χ^2 value of 1.282. The degrees of freedom for this model is 15590. Although this result can be improved further by adding more source components since it is a good result and we are not

continuing our research on this system, we settle with the current model.

Figure 3.1 presents the comparison of our one-component model with the observation for this system.

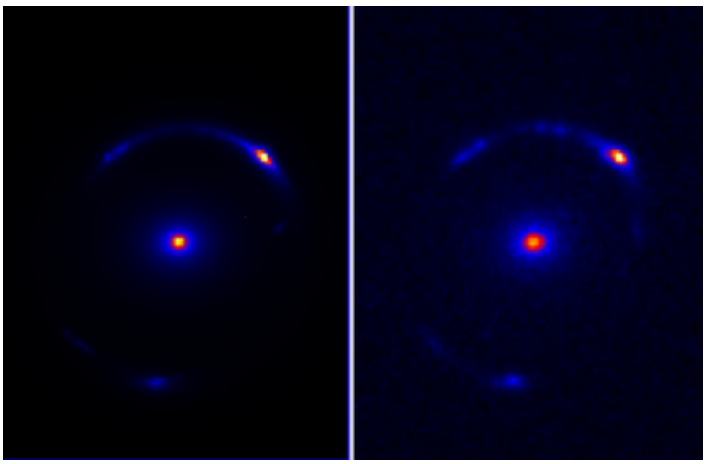

FIGURE 3.1: The left panel corresponds to our best-fit model as per one-component modeling of the target system SDSSJ002927.38+254401.7 while the right panel is the actual HST image of the target system

Best-fit parameter values for this model

Considering the current best fit model, we obtain the following results for parameters. σ is velocity dispersion, e is ellipticity, P.A is position angle, R_{eff} is the effective radius, γ is strength, and ϕ_γ is the polar angle of the external shear, R_{ein} is the Einstien radius, n is the Sérsic index. The cutout image of this target system is not oriented North-up as we wanted it to orient the way it appears in Figure 3.1. Since the position angle is measured east of north according to the image, we expect an offset between the position angles if the observation is actually oriented North-up. The best-fit lens and source parameters are summarized in Tables 3.1 and 3.2

TABLE 3.1: Lens parameters for one-component model of Target SDSSJ002927.38+254401.7

Lens Component	σ (km s^{-1})	Flux (counts)	e	P.A (degrees)	R_{eff} (arcsec)	R_{ein} (arcsec)	n
SIE	270.59	-	0.390	77.05	-	1.32	-
Sérsic	-	29.60	0.219	98.68	0.817	-	4.10

The external shear strength is $\gamma = 0.0011$ and polar angle is $\phi_\gamma = 16.50$ degrees.

TABLE 3.2: Source parameters for one-component model of Target SDSSJ002927.38+254401.7

Source Component	z_S	Flux (counts)	e	P.A (degrees)	$R_{\rm eff}$ (arcsec)	n
Sérsic 1	2.4504	8.60	0.104	125.72	0.281	4.16
Sérsic 2	2.4504	6.40	0.946	129.45	0.011	1.84
Sérsic 3	2.4504	3.82	0.940	92.30	0.007	1.38

Markov Chain Monte Carlo (MCMC) Analysis

We perform MCMC analysis on our results to explore the parameter space and obtain uncertainties in the model parameters. This analysis also helps us detect parameter degeneracies. The MCMC analysis result for some important lens parameters is shown in Figure 3.2.

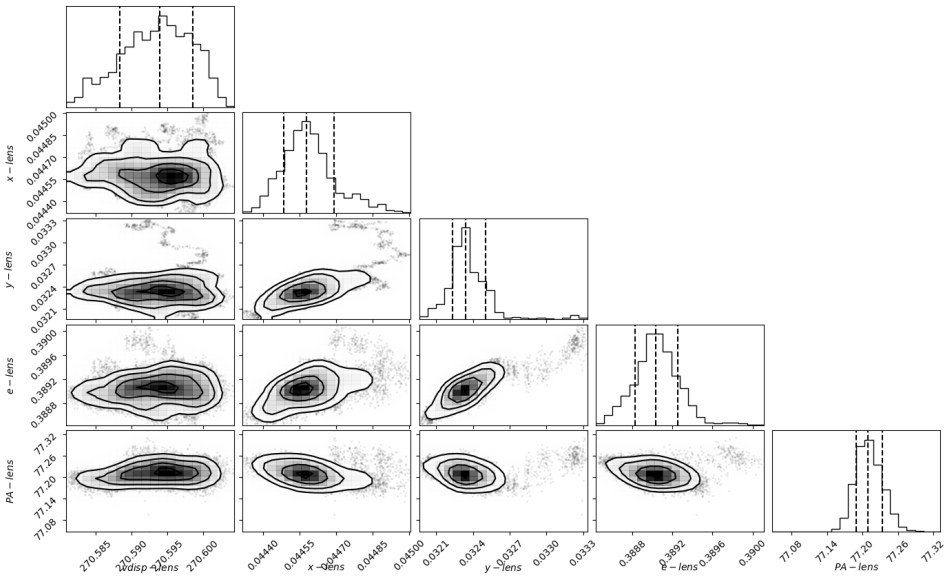

FIGURE 3.2: The marginal posterior distributions for the lens parameters of Target SDSSJ002927.38+254401.7 for one-component model

From Figure 3.2, we can see a parameter degeneracy between ellipticity and the position of the lens. We can perform a better MCMC analysis to find the correlation between other parameters and verify the current correlation.

3.1.2 Two-Component Model

In this model, the stellar mass distribution is modeled using the Hernquist profile and dark matter distribution is modeled with NFW profile. An external shear component is present in the model. The light profile of lens and source components are modeled using the Sérsic profile. We allow offsets between the position, ellipticity, position angle of mass, and light profile of the lens. We also allow offset between centroids of stellar and dark matter distribution. The multiple arcs are modeled considering multiple source components, i.e., Sérsic components at the same redshift. It is found that three Sérsic components for the source light profile can cover all the system's main features. Sérsic indices for all components are kept as free variables during optimization.

As per our current best fit model, after optimizing parameters, we obtain a reduced χ^2 value of 1.280. The degrees of freedom for this model is 15574. This result can be improved further by adding more source components, but since it is a good result and we are not continuing our research on this system, we settle with the current model.

Figure 3.3 presents the comparison of our two-component model with the observation for this system.

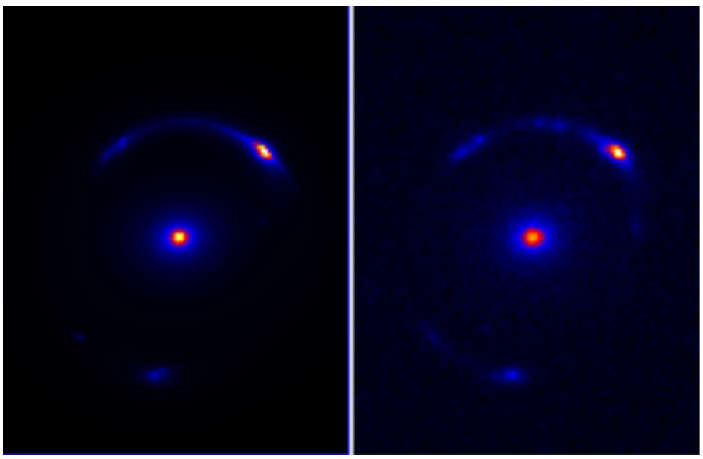

FIGURE 3.3: The left panel corresponds to our best-fit model as per two-component modeling of the target system SDSSJ002927.38+254401.7 while the right panel is the actual HST image of the target system

Best-fit parameter values for this model

The best-fit lens and source parameters are summarized in Tables 3.3 and 3.4.

TABLE 3.3: Lens parameters for the two-component model of Target SDSSJ002927.38+254401.7

Lens Component	M ($M_\odot$)	Flux (counts)	e	P.A (degrees)	R_{ein} (arcsec)	n	R_b or R_{eff} or c
Hernquist	5.41×10^{11}	-	0.210	92.67	1.0885	-	0.437
Sérsic	-	24.38	0.210	92.67	-	3.97	0.793
NFW	5.41×10^{12}	-	0.654	74.20	0.816	-	6.535

The external shear strength is $\gamma = 0.0131$ and polar angle is $\phi_\gamma = 3.138$ degrees.

TABLE 3.4: Source parameters for the two-component model of Target SDSSJ002927.38+254401.7

Source Component	z_S	Flux (counts)	e	P.A (degrees)	R_{eff} (arcsec)	n
Sérsic 1	2.4504	7.05	0.101	308.41	0.285	3.90
Sérsic 2	2.4504	13.07	0.945	134.88	0.011	2.10
Sérsic 3	2.4504	4.04	0.945	74.30	0.011	1.50

M corresponds to the total mass. The last column of Table 3.3 gives values for the parameter scale radius R_b (arcsec) for the Hernquist profile, the effective radius R_{eff} (arcsec) for the Sérsic profile, concentration parameter $c = r_{vir}/r_s$ where r_{vir} is virial radius and r_s is scale radius. The combined effect of both Hernquist and NFW profiles gives us $R_{ein} = 1.33$ arcsec.

The MCMC analysis result for some important lens parameters is shown in Figure 3.4.

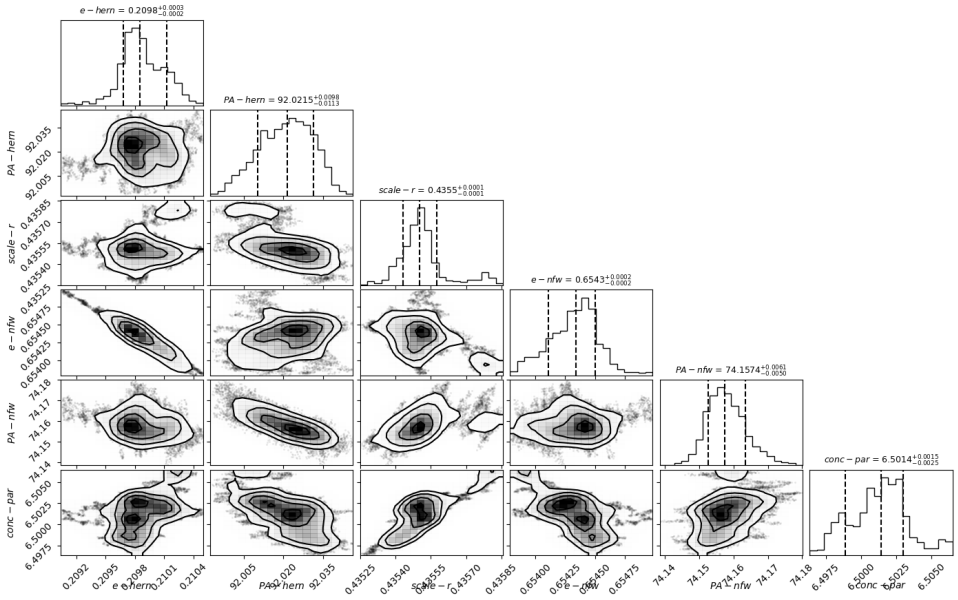

FIGURE 3.4: The marginal posterior distributions for the lens parameters of Target SDSSJ002927.38+254401.7 for the two-component model

From Figure 3.4, we can see that there is an anti-correlation between ellipticities and position angles of Hernquist and NFW profile. We can perform a better MCMC analysis to find the correlation between other parameters and verify the current correlations.

3.1.3 Center and Shape of Mass Distributions

Considering the lens center to be (0,0) in the actual image and allowing the lens center to be a free parameter in modeling, for the two-component model, we get

TABLE 3.5: Parameter comparison of Hernquist (stellar) and NFW (dark matter) profile

Lens Component	x (arcsec)	y (arcsec)	e	P.A (degrees)
Hernquist	0.0160	-0.1332	0.210	92.04
NFW	0.0669	0.3234	0.653	74.20

From Table 3.5, we can see that the difference in position angles of stellar and dark matter distribution is $\sim$18 degrees. Hence we can say that the distributions are reasonably well

aligned. The ellipticity, on the other hand, is significantly different. The dark matter distribution is more elongated than the stellar mass distribution. Due to this difference in the shape of mass distributions, analyzing this feature further is a possible research direction.

3.1.4 Density Profiles

We plot the circular-averaged convergence [1] as a function of the radius to analyze the density profiles according to our models. The convergence is computed with the center at the centroid of the profile and for the source redshift of 2.4504 in a range of radii between 0.1 and 10 arcsec, with a logarithmic interval. The Einstein radius plotted in Figure 3.5 is the average value of what we get considering one and two-component models.

FIGURE 3.5: Average Convergence vs Radius log-log Plot

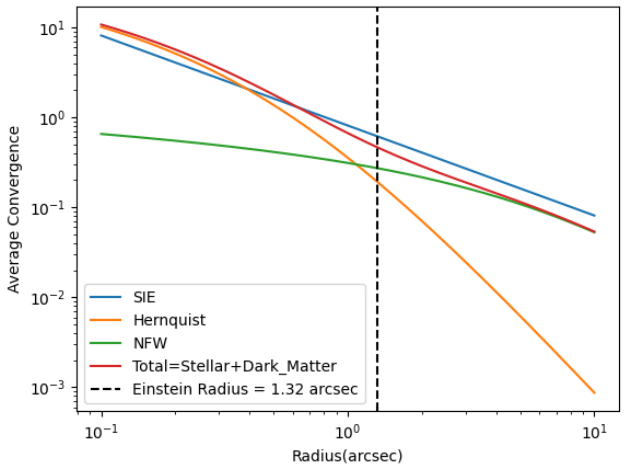

The result shown in Figure 3.5 indicates that our model gives almost the same contribution from Hernquist (stellar) and NFW (dark matter) profiles near Einstein radius, as expected. We obtain convergence of SIE profile at Einstein radius to be 0.61. The figure provides a good overview of the mass distribution as a function of radius.

[1] Convergence is a measure of integrated mass density and is given by the ratio of surface mass density Σ to critical surface mass density Σ_{cr}. Refer footnote 1.

3.2 Double Source Plane System - *Eye of Horus*

The cutout size of the images of this system is 269 $\times$ 163 pixels such that it covers the target system completely and crops out background objects. The pixel size is 0.05 arcsec which is consistent with the pixel size of the instrument HST used to observe this system. We successfully perform both one and two-component modeling on the *Eye of Horus*. While one-component modeling on this system was done by Tanaka et al.(2016) [2], they have done modeling on the image observed by ground-based telescope Hyper Suprime-Cam (HSC) whereas we model the system based on its HST (space-based telescope) image which is deeper and of higher-resolution that allow us to better analyze the features of the system.

3.2.1 One-Component Model

Lens modeled using SIE profile

We first try modeling the lens mass distribution using SIE and external shear. It is found that reproducing both inner and outer arcs at required positions is not possible simultaneously. There is a trade-off between the accuracy of the source 1 (S1) and 2 (S2) arcs considering the mass distribution of the lens. We find that for our best-fit model for this model the Einstein radius for the source is lower than expected. This implies that the density profile of the main lens must be much shallower than the SIE profile. Hence, we next model the lens mass distribution using a power-law model.

Lens modeled using Power-law profile

In this model, the lens mass distribution is modeled using a power-law profile (POW) with external shear. The light profiles of lens and source components are modeled using Sérsic profile. We match the position, set no prior on ellipticity and match the position angle with ratio 1.0 and 1.0 tolerance [2], of lens and its Sérsic profile as well as source 1 mass component and its Sérsic component. This is done as we expect that mass and light distribution have same centroid but their ellipticities can vary, whereas they have to be alligned within 10-20 degrees error in position angle. Sérsic indices for all components are kept as free variables during optimization. There is a flat prior set on shear strength such that it ranges from 0.0

[2] e.g. If parameters 1 (p[1]) and 2 (p[2]) are matched with ratio 0.7 and 0.5 tolerance, it means that p[1] $-$ 0.7 $\times$ p[2] is assumed to have a Gaussian prior with an error of 0.5

to 0.3 which is what we physically expect in such target systems. The velocity dispersion of satellite galaxy mass component is allowed to range between 10 to 100 km s^{-1}, and the velocity dispersion of source 1 mass component ranges between 100 to 240 km s^{-1}. The values of the range for these prior are decided according to an educated guess taken after considering the relevant lensed images positions and Einstein radius. A Gaussian prior with an error of 0.05 and 0.02 arcsec is imposed on the position of the lens and satellite galaxy, respectively, during optimization.

Both the one-component model and two-component model include two external shear components at each lensing object (i.e., lens and source 1) redshift. Source 1 is modeled using SIE profile. The satellite galaxy is centered around (-4.101, 0.419) arcseconds with Gaussian prior, and its mass distribution is modeled using the SIS profile. One Sérsic component is used to model the inner arcs of lensed S1 Three Sérsic components are used to model the A-E features along with reproducing the resolved B feature (i.e., upon careful observation of the HST image (right panel) in Figure 3.6, we can see that there are about three blobs at B feature location of which two are close by, and the third is a far from them) to certain extend. One Sérsic component is used to model the G H features of S2.

As per our current best fit model, after optimization of parameters, we obtain reduced χ^2 value of 1.512. The degrees of freedom for this model is 43787. This result can be improved further by adding more source components, but since it is a good result that reproduces all the system's main features, we settle with the current model.

FIGURE 3.6: The left panel corresponds to the actual HST image of the target system. Our best-fit model as per one-component modeling of the target system Eye of Horus is presented in middle panel, while the right panel is the residual image

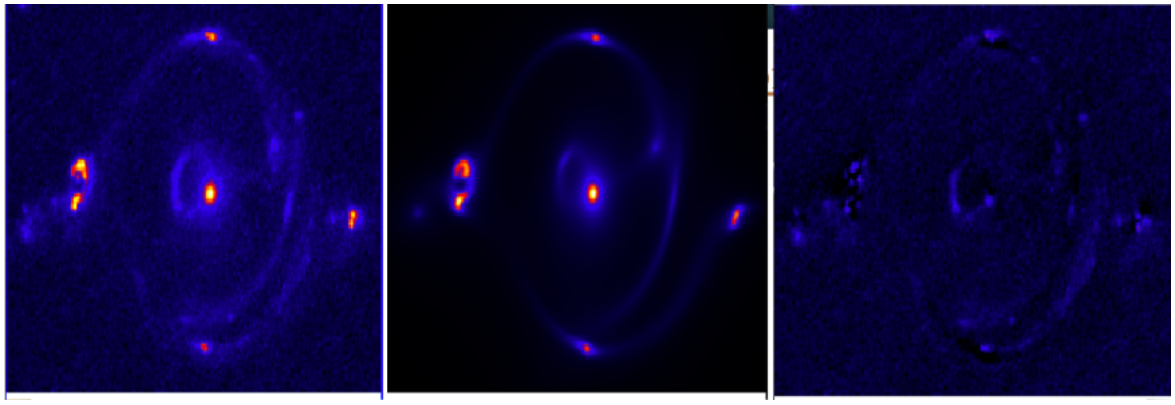

Figure 3.6 presents the comparison of our one-component model with the observation for this system.

Best-fit parameter values for this model

The cutout image of this target system is not oriented North-up as we want it to orient the way it appears in Figure 3.6. Since the position angle is measured east of north according to the image, we expect an offset between the position angles if the observation is actually oriented North-up. The best-fit lens and source parameters are summarized in Tables 3.6 and 3.7

TABLE 3.6: Lens parameters for the one-component model of *Eye of Horus*

Lens Component	σ (km s^{-1})	Flux (counts)	e	P.A (degrees)	R_{eff} (arcsec)	R_{ein} (arcsec)	n or pow index
POW	-	-	0.147	231.000	-	2.044	1.756
Sérsic	-	14.761	0.103	228.301	5.455	-	4.987
Satellite Galaxy	88.826	-	-	-	-	-	
SIE - S1	166.602	-	0.6945	163.639	-	-	-

For external shear component at $z = 0.795$, shear strength is $\gamma = 0.060$ and polar angle is $\phi_\gamma = 184.900$ degrees. For external shear component at z =1.302, shear strength is $\gamma = 0.254$ and polar angle is $\phi_\gamma = 153.989$ degrees.

TABLE 3.7: Source parameters for the one-component model of *Eye of Horus*

Source Component	z_S	Flux (counts)	e	P.A (degrees)	$R_{\rm eff}$ (arcsec)	n
S1-Sérsic 1	1.302	0.293	0.829	150.405	1.211	2.947
S2(A-E)-Sérsic 1	1.990	5.747	0.864	103.771	0.377	4.181
S2(A-E)Sérsic 2	1.990	10.093	0.716	127.562	0.059	2.977
S2(A-E)Sérsic 3	1.990	7.816	0.850	96.230	0.077	3.446
S2(G and H)Sérsic 1	1.990	0.607	0.679	121.669	4.081	4.250

We find that the total lens mass distribution is indeed shallower than SIE ($\rho \propto r^{-2}$) profile. The mass profile with $\rho \propto r^{-1.756}$ is preferred by the best-fit model, indicating the large dark matter fraction, later verified by our two-component model. According to our model the Einstein radius for S1 is 1.998 arcsec and for S2 is 3.864 arcsec.

The MCMC analysis result for some important lens parameters is shown in Figure 3.7. From Figure 3.7, we can see that there is a parameter degeneracy between the power-law

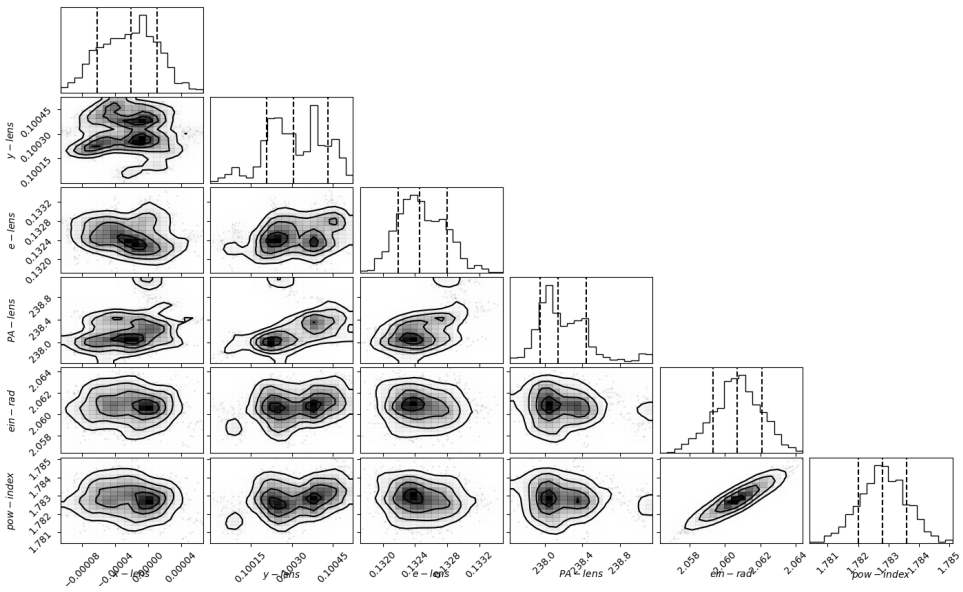

FIGURE 3.7: The marginal posterior distributions for the lens parameters of the one-component model of *Eye of Horus*

index and Einstein radius. We can perform a better MCMC analysis to see the correlation between other parameters.

3.2.2 Two-Component Model

In this model, the stellar mass distribution is modeled using the Hernquist profile and dark matter distribution is modeled with NFW profile. Rest of the model and priors are kept same as the one-component model. We allow offset in the centre of the mass distributions. Since the system is present in a cluster environment, no prior on relative masses of stellar and dark matter components is applied.

As per our current best fit model, after optimization of parameters, we obtain reduced χ^2 value of 1.464. The degrees of freedom for this model is 43781. This result can be improved further by adding more source components but since it is a good result that reproduces all the system's main features, we settle with the current model.

Figure 3.8 presents the comparison of our two-component model with the observation for this system.

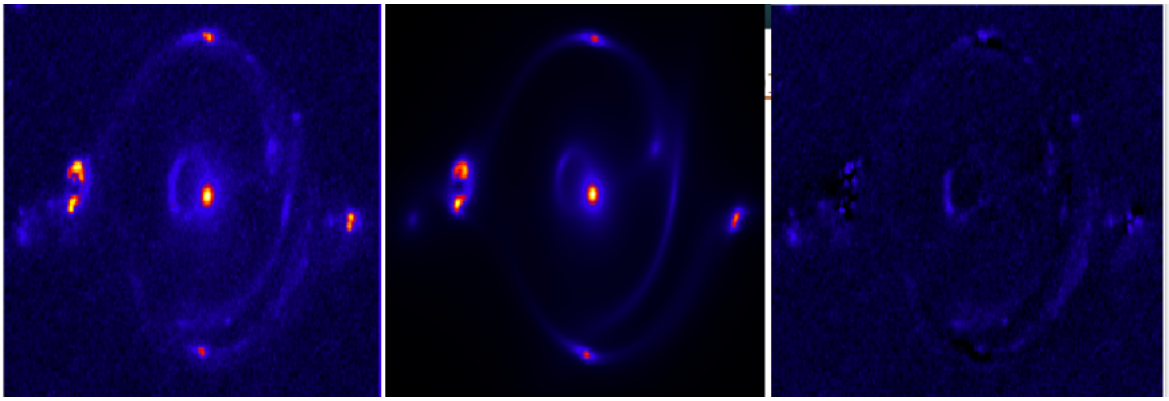

FIGURE 3.8: The left panel corresponds to the actual HST image of the target system. Our best-fit model as per two-component modeling of the target system Eye of Horus is presented in middle panel, while the right panel is the residual image

Best-fit parameter values for this model

The best-fit lens and source parameters are summarized in Tables 3.8 and 3.9

M corresponds to the total mass. The last column of Table 3.3 gives values for parameter scale radius R_b (arcsec) for Hernquist profile, effective radius R_{eff} (arcsec) for Sérsic profile, concentration parameter $c = r_{vir}/r_s$ where r_{vir} is virial radius and r_s is scale radius.

TABLE 3.8: Lens parameters for two-component model of *Eye of Horus*

Lens Component	M ($M_\odot$)	Flux (counts)	e	P.A (arcsec)	n	R_b or R_{eff} or c
Hernquist	1.298×10^{12}	-	0.101	348.637	-	0.942
Sérsic	-	24.38	0.101	350.118	5.136	5.509
NFW	6.382×10^{13}	-	0.177	50.262	-	10.096
Satellite Galaxy	92.884	-	-	-	-	
SIE - S1	201.023	-	0.698	165.582	-	-

According to our model, the Einstein radius for S1 is 2.110 arcsec and for S2 is 3.854 arcsec.

For external shear component at $z = 0.795$, shear strength is $\gamma = 0.058$ and polar angle is $\phi_\gamma = 184.277$ degrees. For external shear component at $z = 1.302$, shear strength is $\gamma = 0.273$ and polar angle is $\phi_\gamma = 157.146$ degrees.

TABLE 3.9: Source parameters for the two-component model of the *Eye of Horus*

Source Component	z_S	Flux (counts)	e	P.A (degrees)	R_{eff} (arcsec)	n
S1-Sérsic 1	1.302	0.332	0.797	150.8625	-	2.976
S2(A-E)-Sérsic 1	1.990	4.149	0.876	104.735	0.158	3.291
S2(A-E)Sérsic 2	1.990	7.787	0.748	126.738	0.034	2.367
S2(A-E)Sérsic 3	1.990	8.3340.813	100.463	0.095	3.378	
S2(G and H)Sérsic 1	1.990	0.518	0.710	117.6389	5.469	4.307

The MCMC analysis result for some important lens parameters is shown in Figure 3.9.

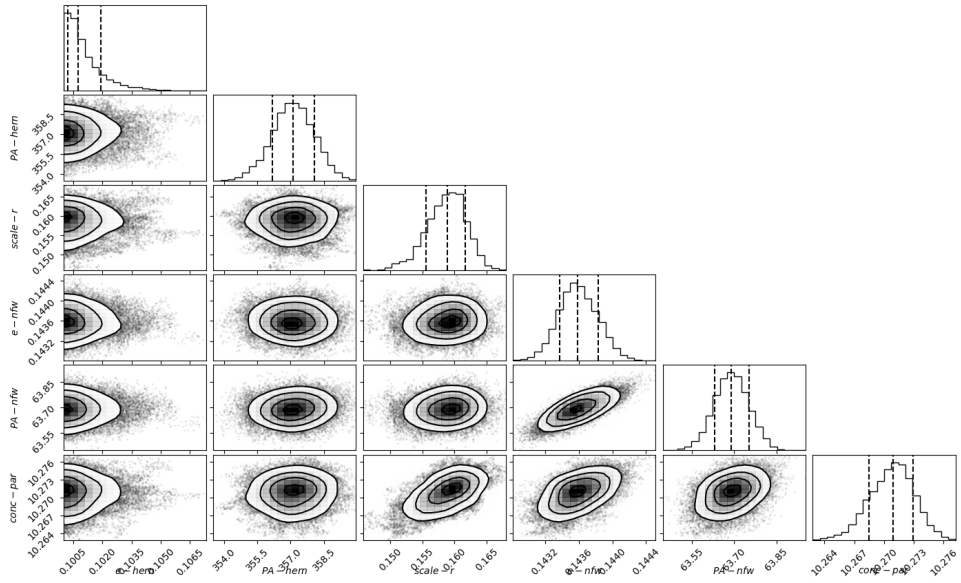

FIGURE 3.9: The marginal posterior distributions for the lens parameters of the two-component model of the *Eye of Horus*

From Figure 3.9, we can see that there is a parameter degeneracy between ellipticity and position angle of the NFW profile. Upon careful analysis, we expect a correlation between ellipticity and the position angle of the Hernquist profile too. We can perform a better MCMC analysis to see a correlation between the mass of the profiles and other parameters.

3.2.3 Center and Shape of Mass Distributions

Considering the lens center to be (0.5832, 0.0725) in the actual image and allowing the lens center to be a free parameter with a Gaussian prior in modeling, for the two-component model we find that the centroids of the two mass distributions have some offset. Though it is about 0.15 arcseconds, it is quite large for galaxy-scale lens. This might indicate that the cluster mass is contributing quite a bit to the lensing.

TABLE 3.10: Parameter comparison of the Hernquist (stellar) and NFW (dark matter) profile

Lens Component	x (arcsec)	y (arcsec)	e	P.A (degrees)
Hernquist	0.5812	0.0674	0.101	348.637
NFW	0.5048	0.2014	0.177	50.262

From Table 3.10, we can see that the difference in position angles of stellar and dark matter distribution is ~ 61.625 degrees. Hence we can say that the distributions are misaligned. Due to cluster environment and external shear, we did expect misalignment in the mass distributions, but the magnitude of misalignment that we get from our lensing model is quite a lot and lies at the extreme end of error allowed as per Horizon-AGN simulation analyzed at mass scale $\sim 10^{13}$ by [35]. On the other hand, the ellipticities are almost similar and lie within the error bar of what is expected according to Horizon-AGN simulation [36, 37]. However, if we precisely compare the shape of the two profiles, we find that the dark matter distribution is more elongated than the stellar mass distribution.

In the literature, if we focus on two studies that were done on the shape comparison of the stellar and dark matter distributions, we find that our result on the shape comparison of the mass distributions that claim that dark matter distribution is more elongated than the stellar mass distribution is consistent with Okabe et al. 2020 [35] while is in contrast with Bruderer et al. 2016 [38] which claims that dark matter haloes are rounder than the stellar mass distribution. The inconsistencies in the comparison of the result on shape comparison might be due to several reasons. We are estimating ellipticities within the Einstein radius whereas the radius scale that the other two studies work at is different, and it is believed that the ellipticities have some radial dependence [35, 39], so if we probe at different radius scales, for example, at the cluster scale then, we are probing a different region and might expect different ellipticities. Another possible reason is the mass dependency of ellipticities [35]. We are working with a system with lens that has total mass $\sim 10^{13} M_{\odot}$, whereas the target systems that the other two studies are based upon are of different mass scales. Therefore, to get robust results on shape comparison of mass distributions, we need to analyze samples at different mass scales and perform simulations at larger box sizes such that we could draw a better correlation between ellipticities and their mass and radial dependence. Then we would be able to get better conclusions on the shape comparison. Other possibilities of inconsistencies are that our modeling techniques (e.g., profiles used to model the lenses), the definition of ellipticities in the model, methods of estimating ellipticities are different, so to draw a conclusion considering other studies, we need to come to common grounds.

3.2.4 Density Profiles

We plot the circular-averaged convergence as a function of the radius to analyze the density profiles according to our models. The convergence is computed with the center at the centroid of the profile and for the source redshift 1.990 in a range of radii between 0.1 and 10 arcsec, with a logarithmic interval. The Einstein radii plotted on graph are the average value of what we get considering one and two-component models.

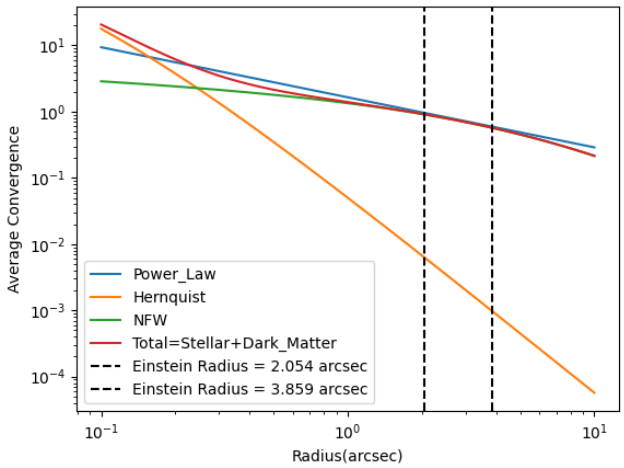

FIGURE 3.10: Average Convergence vs Radius log-log Plot

The result shown in Figure 3.10 indicates that the dark matter dominates over stellar mass around both the Einstein radius confirming our prediction from the density profile estimate of the lens which was found to be shallower than SIE profile . We suppose this is due to the fact that the *Eye of Horus* is located in a massive cluster. A good overview of the various mass distributions against radius can be inferred from Figure 3.10

3.2.5 Initial Mass Function

We compare the stellar mass derived from our lensing model with the stellar mass estimated in [2] using MIZUKI (that uses five-band photometry, known redshift of the lens galaxy and fits a spectral energy distribution (SED) using MIZUKI with a suite of model templates that assume the Chabrier IMF). The stellar mass of $6.6\times10^{11}M_{\odot}$ is estimated by MIZUKI, while we get $12.98\ \times10^{11}M_{\odot}$. Our stellar mass estimate is offset by a factor of two, suggesting that Salpeter IMF provides a better description of the stellar population of the lens.

Chapter 4

Summary

We have successfully done the first two-component modeling on the Hubble space telescope images of the target systems SDSSJ002927.38+254401.7 selected from the BELLS GALLERY sample and the interesting double source plane lensed system *Eye of Horus*.

Focusing on the main lens system *Eye of Horus*, we find that the lensing galaxy of the *Eye of Horus* follows a power-law radial density profile ($\rho \propto r^{-\gamma}$) with $\gamma = 1.7559$, which is shallower than the SIE profile. Our results are consistent with [2] that had found a shallower profile for the lens and suggested a large dark matter fraction in this system. We verified the large dark matter fraction within the Einstein radius using the circularly-averaged convergence against the radius (see Figure 3.10). We assume a satellite galaxy at the same redshift as the lens galaxy to be the mass component between the features A and C that splits them into two images. The velocity dispersion of this satellite galaxy, assuming an SIS profile, is $\sim$93 km s^{-1}. For the source 1, we find velocity dispersion of 201 km s^{-1} (assuming an SIE profile). Some parameter degeneracies were detected in the model. We plan to explore more of these by conducting an improved MCMC analysis of the best-fit model. Our current one and two-component models for both the systems reproduce all the important features of the lensed systems

In both the systems, it was found that the dark matter distribution was more elongated than the stellar mass distribution. This result is in agreement with [35] and in disagreement with [38]. This might be due to the mass scale differences of the target systems or the modeling limitations. We need to model our systems considering parameter degeneracies and MCMC analysis. Modeling more such double source plane systems or multiple strong lens

systems is important to draw more robust conclusion on shape comparison of the stellar and dark matter distributions.

The dark and stellar mass distributions of the target SDSSJ002927.38+254401.7 were found to be well aligned . On the other hand the dark and stellar mass distributions of *Eye of Horus* had a large offset in the position angles. The cluster environment of *Eye of Horus* is a possible reason for the misalignment. We need to increase our target sample size and carefully consider external perturbation (including higher order perturbation) in the current model to improve the result on the alignment of the stellar and dark matter distributions.

The stellar mass for the foreground lens was found to be 12.98 $\times 10^{11} M_{\odot}$. After comparing this with the stellar mass (6.6 $\times 10^{11} M_{\odot}$) inferred from stellar population synthesis fitting (which assume Chabrier IMF) we find that a Salpeter IMF provides a better description of the stellar population of the lens. This is in agreement with [40–42], which suggest that Salpeter IMF provides stellar masses in agreement with those inferred by lensing whereas Chabrier IMF underestimates them.

Our detailed model for the double source plane lensed system *Eye of Horus* could further be used in various directions such as constraining cosmological parameters, looking for constraints on galaxy formation in ΛCDM using the shape comparison of stellar and dark matter distributions, and studying the initial mass functions of early type galaxies.

Bibliography

[1] Shyuichi Izumiya and S Janeczko. A symplectic framework for multiplane gravitational lensing. *Journal of Mathematical Physics*, 44(5):2077–2093, 2003.

[2] Masayuki Tanaka, Kenneth C Wong, Anupreeta More, Arsha Dezuka, Eiichi Egami, Masamune Oguri, Sherry H Suyu, Alessandro Sonnenfeld, Ryo Higuchi, Yutaka Komiyama, et al. A spectroscopically confirmed double source plane lens system in the hyper suprime-cam subaru strategic program. *The Astrophysical Journal Letters*, 826(2):L19, 2016.

[3] Keigo Tanaka, Ayumi Tsuji, Hiroki Akamatsu, JHH Chan, Jean Coupon, Eiichi Egami, Francois Finet, Ryuichi Fujimoto, Yuto Ichinohe, Anton T Jaelani, et al. X-ray study of the double source plane gravitational lens system eye of horus observed with xmm–newton. *Monthly Notices of the Royal Astronomical Society*, 491(3):3411–3418, 2020.

[4] Ramesh Narayan and Matthias Bartelmann. Lectures on gravitational lensing. *arXiv preprint astro-ph/9606001*, 1996.

[5] Massimo Meneghetti. Introduction to gravitational lensing–lecture scripts. *research-gate. net/publication/310620466*, 2016.

[6] P Schneider. P., j. ehlers, ee falco. *Gravitational Lenses*, 1992.

[7] G Bertin, F Bertola, LM Buson, IJ Danzinger, Herwig Dejonghe, EM Sadler, RP Saglia, PT De Zeeuw, and WW Zeilinger. A search for dark matter in elliptical galaxies: radially extended spectroscopic observations for six objects. *Astronomy and Astrophysics*, 292:381–391, 1994.

[8] Tommaso Treu. Strong lensing by galaxies. *Annual Review of Astronomy and Astrophysics*, 48:87–125, 2010.

[9] JD Remolina González, K Sharon, B Reed, N Li, G Mahler, LE Bleem, M Gladders, A Niemiec, A Acebron, and H Child. Efficient mass estimate at the core of strong lensing galaxy clusters using the einstein radius. *The Astrophysical Journal*, 902(1):44, 2020.

[10] Andrea V Maccio, Aaron A Dutton, Frank C Van Den Bosch, Ben Moore, Doug Potter, and Joachim Stadel. Concentration, spin and shape of dark matter haloes: scatter and the dependence on mass and environment. *Monthly Notices of the Royal Astronomical Society*, 378(1):55–71, 2007.

[11] Victor P Debattista, Ben Moore, Thomas Quinn, Stelios Kazantzidis, Ryan Maas, Lucio Mayer, Justin Read, and Joachim Stadel. The causes of halo shape changes induced by cooling baryons: disks versus substructures. *The Astrophysical Journal*, 681(2):1076, 2008.

[12] Robert Kormann, Peter Schneider, and Matthias Bartelmann. Isothermal elliptical gravitational lens models. *Astronomy and Astrophysics*, 284:285–299, 1994.

[13] Nicolas Tessore and R. Benton Metcalf. The elliptical power law profile lens. *Astronomy &amp Astrophysics*, 580:A79, aug 2015.

[14] Tommaso Treu and Philip J Marshall. Time delay cosmography. *The Astronomy and Astrophysics Review*, 24(1):1–41, 2016.

[15] Eric V Linder. Doubling strong lensing as a cosmological probe. *Physical Review D*, 94(8):083510, 2016.

[16] Alessandro Sonnenfeld, Tommaso Treu, Raphael Gavazzi, Philip J Marshall, Matthew W Auger, Sherry H Suyu, Leon VE Koopmans, and Adam S Bolton. Evidence for dark matter contraction and a salpeter initial mass function in a massive early-type galaxy. *The Astrophysical Journal*, 752(2):163, 2012.

[17] Peter Schneider. Can one determine cosmological parameters from multi-plane strong lens systems? *Astronomy & Astrophysics*, 568:L2, 2014.

[18] Thomas E Collett, Matthew W Auger, Vasily Belokurov, Philip J Marshall, and Alex C Hall. Constraining the dark energy equation of state with double-source plane strong lenses. *Monthly Notices of the Royal Astronomical Society*, 424(4):2864–2875, 2012.

[19] Thomas E Collett and Matthew W Auger. Cosmological constraints from the double source plane lens sdssj0946+ 1006. *Monthly Notices of the Royal Astronomical Society*, 443(2):969–976, 2014.

[20] Raphael Gavazzi, Tommaso Treu, Léon VE Koopmans, Adam S Bolton, Leonidas A Moustakas, Scott Burles, and Philip J Marshall. The sloan lens acs survey. vi. discovery and analysis of a double einstein ring. *The Astrophysical Journal*, 677(2):1046, 2008.

[21] H Tu, R Gavazzi, M Limousin, R Cabanac, PJ Marshall, B Fort, T Treu, R Péllo, E Jullo, J-P Kneib, et al. The mass profile of early-type galaxies in overdense environments: the case of the double source-plane gravitational lens sl2sj02176-0513. *Astronomy & Astrophysics*, 501(2):475–484, 2009.

[22] Yiping Shu, Adam S Bolton, Shude Mao, Christopher S Kochanek, Ismael Pérez-Fournon, Masamune Oguri, Antonio D Montero-Dorta, Matthew A Cornachione, Rui Marques-Chaves, Zheng Zheng, et al. The boss emission-line lens survey. iv. smooth lens models for the bells gallery sample. *The Astrophysical Journal*, 833(2):264, 2016.

[23] Masamune Oguri, Yen-Ting Lin, Sheng-Chieh Lin, Atsushi J Nishizawa, Anupreeta More, Surhud More, Bau-Ching Hsieh, Elinor Medezinski, Hironao Miyatake, Hung-Yu Jian, et al. An optically-selected cluster catalog at redshift 0.1< z< 1.1 from the hyper suprime-cam subaru strategic program s16a data. *Publications of the Astronomical Society of Japan*, 70(SP1):S20, 2018.

[24] Charles R Keeton and Ann I Zabludoff. The importance of lens galaxy environments. *The Astrophysical Journal*, 612(2):660, 2004.

[25] Edwin E Salpeter. The luminosity function and stellar evolution. *The Astrophysical Journal*, 121:161, 1955.

[26] Gilles Chabrier. Galactic stellar and substellar initial mass function1. *Publications of the Astronomical Society of the Pacific*, 115(809):763, 2003.

[27] AS Fruchter and RN Hook. Drizzle: A method for the linear reconstruction of undersampled images. *Publications of the Astronomical Society of the Pacific*, 114(792):144, 2002.

[28] Charles R Keeton. A catalog of mass models for gravitational lensing. *arXiv preprint astro-ph/0102341*, 2001.

[29] Nicolas Tessore and R Benton Metcalf. The elliptical power law profile lens. *Astronomy & Astrophysics*, 580:A79, 2015.

[30] Lars Hernquist. An analytical model for spherical galaxies and bulges. *The Astrophysical Journal*, 356:359–364, 1990.

[31] Julio F Navarro, Carlos S Frenk, and Simon DM White. A universal density profile from hierarchical clustering. *The Astrophysical Journal*, 490(2):493, 1997.

[32] John Krist. Simulation of hst psfs using tiny tim. In *Astronomical Data Analysis Software and Systems IV*, volume 77, page 349, 1995.

[33] Masamune Oguri. The mass distribution of sdss j1004 +4112 revisited. *Publications of the Astronomical Society of Japan*, 62(4):1017–1024, 2010.

[34] Masamune Oguri. Fast calculation of gravitational lensing properties of elliptical navarro–frenk–white and hernquist density profiles. *Publications of the Astronomical Society of the Pacific*, 133(1025):074504, 2021.

[35] Taizo Okabe, Masamune Oguri, Sébastien Peirani, Yasushi Suto, Yohan Dubois, Christophe Pichon, Tetsu Kitayama, Shin Sasaki, and Takahiro Nishimichi. Shapes and alignments of dark matter haloes and their brightest cluster galaxies in 39 strong lensing clusters. *Monthly Notices of the Royal Astronomical Society*, 496(3):2591–2604, 2020.

[36] Yohan Dubois, Christophe Pichon, Charlotte Welker, Damien Le Borgne, Julien Devriendt, Clotilde Laigle, Sandrine Codis, Dmitry Pogosyan, Stéphane Arnouts, Karim Benabed, et al. Dancing in the dark: galactic properties trace spin swings along the cosmic web. *Monthly Notices of the Royal Astronomical Society*, 444(2):1453–1468, 2014.

[37] Taizo Okabe, Takahiro Nishimichi, Masamune Oguri, Sébastien Peirani, Tetsu Kitayama, Shin Sasaki, and Yasushi Suto. Projected alignment of non-sphericities of stellar, gas, and dark matter distributions in galaxy clusters: analysis of the horizon-agn simulation. *Monthly Notices of the Royal Astronomical Society*, 478(1):1141–1160, 2018.

[38] Claudio Bruderer, Justin I Read, Jonathan P Coles, Dominik Leier, Emilio E Falco, Ignacio Ferreras, and Prasenjit Saha. Light versus dark in strong-lens galaxies: Dark matter haloes that are rounder than their stars. *Monthly Notices of the Royal Astronomical Society*, 456(1):870–884, 2016.

[39] Brandon Allgood, Ricardo A Flores, Joel R Primack, Andrey V Kravtsov, Risa H Wechsler, Andreas Faltenbacher, and James S Bullock. The shape of dark matter haloes: dependence on mass, redshift, radius and formation. *Monthly Notices of the Royal Astronomical Society*, 367(4):1781–1796, 2006.

[40] Tommaso Treu, Matthew W Auger, Léon VE Koopmans, Raphaël Gavazzi, Philip J Marshall, and Adam S Bolton. The initial mass function of early-type galaxies. *The Astrophysical Journal*, 709(2):1195, 2010.

[41] C Grillo, R Gobat, M Lombardi, and P Rosati. Photometric mass and mass decomposition in early-type lens galaxies. *Astronomy & Astrophysics*, 501(2):461–474, 2009.

[42] MW Auger, T Treu, R Gavazzi, AS Bolton, LVE Koopmans, and PJ Marshall. Dark matter contraction and the stellar content of massive early-type galaxies: Disfavoring "light" initial mass functions. *The Astrophysical Journal Letters*, 721(2):L163, 2010.